

HOSTED BY



ELSEVIER

Contents lists available at ScienceDirect

Journal of King Saud University – Science

journal homepage: www.sciencedirect.com

Original article

Investigation of optical, electrical and magnetic properties of hematite α -Fe₂O₃ nanoparticles via sol-gel and co-precipitation method

Muhammad Tahir^a, M. Fakhar-e-Alam^{a,*}, M. Atif^b, Ghulam Mustafa^c, Zulfiqar Ali^d^a Department of Physics, G. C. University, Faisalabad 38000, Pakistan^b Department of Physics and Astronomy, College of Science, King Saud University, P O Box 2455, Riyadh 11451, Saudi Arabia^c Department of Physics, Bahauddin Zakariya University, Multan 60800, Pakistan^d Department of Mathematics and Physics, University of Campania Luigi Vanvitelli, Viale Abramo Lincoln, 5, 81100 Caserta, Italy

ARTICLE INFO

Article history:

Received 9 September 2022

Revised 27 January 2023

Accepted 15 April 2023

Available online 20 April 2023

Keywords:

Co-precipitation

Sol-gel

Hematite (α -Fe₂O₃)

X-ray diffraction

Dielectric response

AC conductivity

Band gap

M–H loop

ABSTRACT

Hematite (α -Fe₂O₃) nanoparticles were synthesized using co-precipitation and sol-gel methods. X-ray diffraction (XRD) technique was employed to structural properties of the synthesized α -Fe₂O₃ nanoparticles and SEM(scanning electron microscopy) was used to analyze the morphological structure. The crystallite size is determined Sample-A (33 nm) and Sample-B (29 nm) by Scherer formula, while Volume of unit cell is measured 301.8 $\times 10^6$ pm³ and 301.8 $\times 10^6$ pm³ respectively. The X-ray density is found in the Sample-A 5.27 (g/cm³) and Sample-B 5.26 (g/cm³). The optical band gap energy measured 2.4–2.6 eV, calculated by the Tauc plot with the optical absorption data. The electrical characteristics of the samples were examined by using two probe methods and the possible impact of temperature on the electrical properties of α -Fe₂O₃ was investigated. Dielectric analysis reveals an inverse relationship between the permittivity of α -Fe₂O₃ samples and frequency that fulfills the Maxwell Wagner Model. The magnetic parameters were observed Ms = 9.29 emu, 1.72 emu and coercivity Hc = 1404(G) as well as Hc = 1040 (G). The observed values of these factors indicate that the materials can be employed in a variety of applications such as catalysis, sensors and water purification.

© 2023 The Author(s). Published by Elsevier B.V. on behalf of King Saud University. This is an open access article under the CC BY-NC-ND license (<http://creativecommons.org/licenses/by-nc-nd/4.0/>).

1. Introduction

Iron oxides are specifically of great importance due to their wide range applications in magnetic storage, rechargeable lithium batteries, catalysis, absorption at nanoscale (Kanungo et al., 1996). Iron oxides exist naturally in many different forms, hematite (α -Fe₂O₃), maghemite (γ -Fe₂O₃) and magnetite (Fe₃O₄) are most common (Kholam et al., 2002). Among all these types of iron oxides most stable is hematite having corundum structure R3c exhibit weak ferromagnetic pattern. Hematite shows 2.1 eV band gap in bulk form and it's a n-type semiconductor. It has attracted many researchers due to its unique structural, optical, electrical and magnetic properties. Abaker et al., (2011) has synthesized α -Fe₂O₃ nanoparticles. The magnetic and optical properties show

unusual behavior due to crystallite size and shape. (Assefa et al., 2022) has studied the Zn based spinel ferrite nanofibers prepared by electro spinning method. Dawit Gudeta (Gunjo et al., 2022) a paraffin-based nanofluid, blended with aluminum oxide (Al₂O₃) nanoparticles has been studied bio-applications. It can be inferred that combining latent heat storage devices (LHSD) with a solar water heater may be used in technologies such as biogas generation. It is noteworthy, (Nosheen et al., 2022) has been synthesized Al_{0.5}Cr_{0.5}Zn₀Fe₂O₄ and Zn_{0.5}Cr_{0.5}Al₀Fe₂O₄ ferrites via sol-gel auto combustion method. The study showed correlations between coercivity and crystallite size. In the both investigation reports, the materials have numerous applications in electronic, microwave fields and medical appliances. According to (Bahamonde et al., 2018) reports Biosensors are highly selective devices that are being employed in interdisciplinary research that connects the principle of fundamental science with biomedicine. Recent advancements in the field of applications, many methods have been used for the synthesis of iron oxide nano-powders. Now we going to synthesized same compound iron oxide nano-powders with two different methods such as co-precipitation and Sol-gel method. (Mustafa, et al., 2015a, 2015b). Preparation methods and mechanism of crystal growth of Fe₂O₃ nanoparticle has been reported with various shapes like nanowires, nano-plates, nano-rods and cubes and

* Corresponding author.

E-mail address: fakharphy@gmail.com (M. Fakhar-e-Alam).

Peer review under responsibility of King Saud University.



Production and hosting by Elsevier

<https://doi.org/10.1016/j.jksus.2023.102695>

1018-3647/© 2023 The Author(s). Published by Elsevier B.V. on behalf of King Saud University.

This is an open access article under the CC BY-NC-ND license (<http://creativecommons.org/licenses/by-nc-nd/4.0/>).

all the shapes of the materials depend upon the synthetic parameters, such as temperature, pH, Fe^{2+}/Fe^{3+} ratio, annealing temperatures and mild reducing agent. Magnetic nanoparticles towards biomedical applications show excellent potential especially for cancer treatment purpose (Abbas et al., 2022; Alam et al., 2021; Atif et al., 2010, 2011, Fakhar-e-Alam et al., 2020a,b, Hassan et al., 2022a,b; Mahmood et al., 2022).

The aim of current work is to synthesize materials with desirable applications such as $-Fe_2O_3$ nanoparticles at a low cost. It will be enthralling to examine different methodology co-precipitation and Sol-gel and its influence on the structural and optical, dielectrical and magnetic properties. In this study, we investigate hematite ($\alpha-Fe_2O_3$) nanoparticles to better understand the role of various methodologies and their impact on structural, optical, dielectrical, and magnetic properties.

2. Materials and methods

2.1. Samples preparation

Synthesize and characterizations of Iron oxides powders by using the co-precipitation method. The desired product was obtained using a $Fe(NO_3)_3 \cdot 9H_2O$ purity 98%, Sigma Aldrich, and sodium Hydroxide NaOH. 99% pure, Florida. These materials were mixed in the deionized water. NaOH solution was used for maintaining the pH level at 11, magnetic stirrer was used for this process. The precipitate obtained after magnetic stirrer process was digested in a preheated water at 75 °C for 1 h. For removing the byproducts, the precipitate was washed many times through deionized water and ethanol. Last step for getting required product was dry at 90 °C in an electrical oven for 24 h. With the help of mortar, the dried samples were grinded, and annealed at 500 °C for 3 h.

Another way to prepared Iron oxides powders with the Sol-gel method. The $Fe(NO_3)_3 \cdot 9H_2O$ purity 98%, Sigma Aldrich, acetic acid $C_6H_8O_7 \cdot H_2O$, purity 98%, Fisher Scientific, deionized water and ammonia solution (32%) were used to control the pH 7. The prepared $Fe(NO_3)_3 \cdot 9H_2O$ and acetic acid solutions were mixed and heated round about at 80 °C for 3 h, and then suitable amount of ammonia solution (32%) was added to control the pH 7. In this chemical procedure, the sol (or solution) gradually changes towards the formation of a gel. Similar experiment has been employed for variety of sample preparations (Atif et al., 2019; Atif et al., 2021; Fakhar et al., 2022). To obtain the powders were annealed at the same conditions, Pellets of these samples having thickness of 0.30 cm were made using hydraulic press by applying 35 kN load and sintered temperature 500 °C for 3 h. In order to get pallets with smooth surface, these were polished. **The schematic diagram of the both methods sol-gel and co-precipitation is present in the Fig. 1.**

2.2. Characterizing techniques

XRD patterns were acquired at room temperature with powder samples applying an Xpert Pro PANalytical diffractometer with Nickel filtered $Cu-K\alpha$ radiation $\lambda = 1.5405 \text{ \AA}$ for internal structure study. Morphological study of the prepared sample was performed by SEM Manufacturer: JEOL Model: -JSM 5910. The Raman spectroscopy was done by using a Manufacturer company: HORIBA France SAS spectrometer, having argon-ion laser wavelength (623.8 nm). The obtained pattern by Raman spectroscopy was in back-scattering geometry by the powder between 250 and 800 cm^{-1} For optical analysis of the prepared sample, Shimadzu UV-2550 PC UV-Vis Spectrophotometers with wavelength with range from 200 to 1100 nm was used. The dielectric analysis of Iron

oxides samples was obtained at room temperature by using Wayne Ker WK-6500B series precision impedance analyzers instrument. With the help of Vibrating sample magnetometer (VSM) Manufacturer company: Lake Shore Model: 7407 series magnetic properties were measured at room temperature.

The data obtained from XRD analysis was used to measure the physical parameters like lattice constant, volume of a unit cell, crystallite size and X-ray density by these formulas as listed below (Hassan et al., 2022a; Goldman et al., 2006).

$$d = \frac{1}{\sqrt{\frac{4(h^2+hk+k^2)+\frac{c^2}{a^2}}{3a^2}}} \quad (1)$$

$$V_{cell} = \frac{\sqrt{3}}{2} a^2 c \quad (2)$$

$$D = \frac{0.9\lambda}{\beta \cos \theta} \quad (3)$$

$$\rho_{X-ray} = \frac{MZ \times 1.66}{V_{cell}} \quad (4)$$

$$\text{Dislocation density, } \delta = \frac{1}{D^2} \quad (5)$$

$$\text{Microstrain, } \epsilon = \frac{\beta \cot \theta}{4} \quad (6)$$

Where a and c are lattice parameter, V_{cell} is unit cell volume, (hkl) are Miller indices, Z is the number of molecules per unit cell of the structure, NA show Avogadro's number (6.021023 g/mol), and M is molecular weight. The crystallite size (D) nm was calculated using Scherer's formula, as indicated by equation (3), Here K is shape factor, λ is wavelength of X-ray and θ is angle of diffraction.

Lattice strain ϵ and B is the full width at half maximum (FWHM). Here (δ) is represent dislocation density.

The samples were fabricated in the capacitor form for the response of the dielectric characteristics (Dielectric constant (ϵ'), Loss tangent ($\tan \delta$), and AC conductivity) and may be assumed electrically equal to capacitance C_p in parallel with resistance R_p . These values (C_p and R_p) were determined by applying an impedance analyzer, and the electrical parameters were determined by applying the below equations (Graca et al., 2007).

$$\epsilon = \frac{C_0}{C_p} \text{ where } C_0 = \frac{A\epsilon_0}{d} \quad (7)$$

$$\tan \delta = \frac{1}{\omega C_p R_p} \quad (8)$$

$$\sigma_{ac} = \omega \epsilon_0 \epsilon' \tan \delta \quad (9)$$

where C_0 is the capacitance of the given sample in vacuum that completely dependent on the area(A), spacing(d), permittivity (ϵ_0) its value is $8.85 \times 10^{-12} \text{ F/cm}$ and angular frequency (ω) of the applied frequency.

3. Results and discussion

3.1. X-ray diffraction analysis

The comparison of two different methodologies employed to observed structural evolution. The crystalline phases were identified using a (XRD) X-ray diffractometer for the structural analysis. Fig. 1 reveals the XRD patterns, Sample-A Iron oxides prepared by

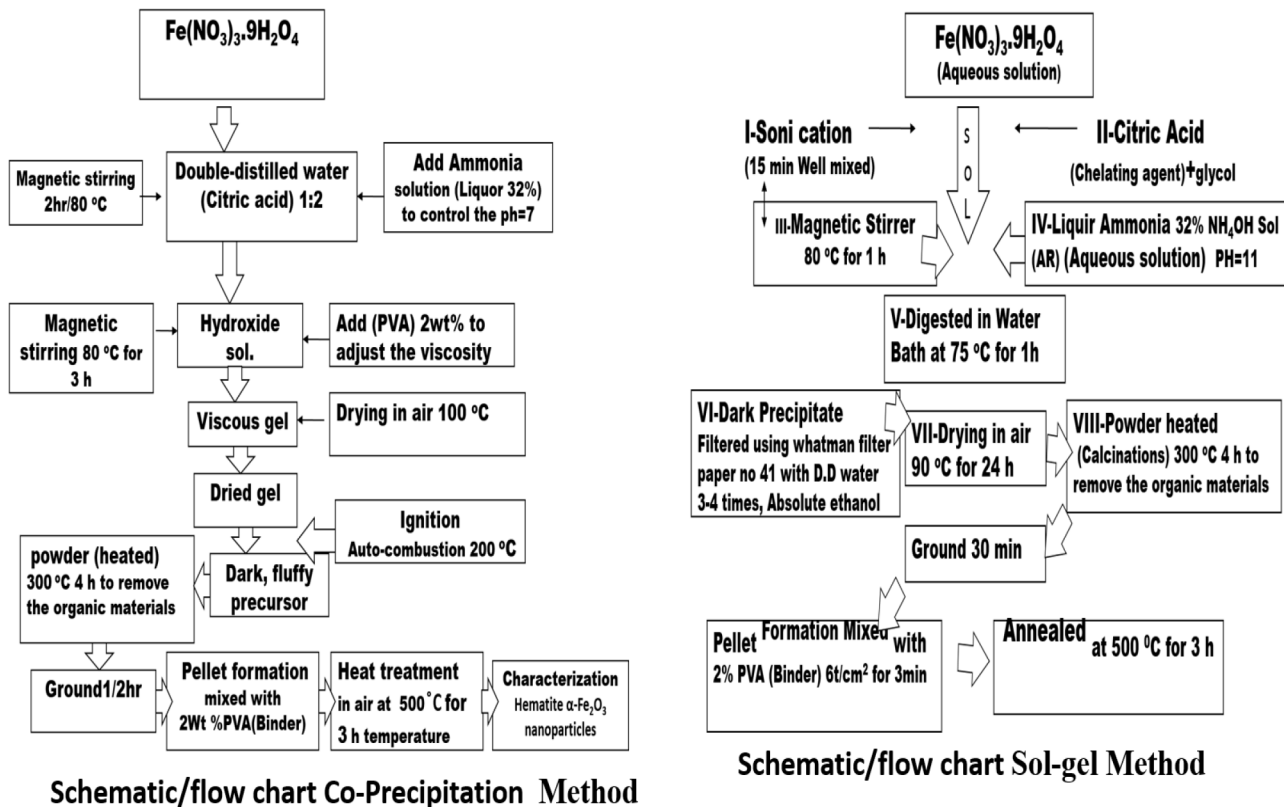


Fig. 1. Schematic diagram of the sol-gel and co-precipitation method.

using co-precipitation method while Sample-B synthesized by another way Sol-gel method. Diffracted peaks were indexed according to (Chaudhari, et al., 2009) reported that samples have the rhombohedral structure of hematite α - Fe_2O_3 , which were in similarity with JCPDS no.33-0664. The sharp diffracted peaks exhibited completely crystallinity of the given samples reported by (Mustafa et al., 2015a, 2015b). The peak location $2\theta = 33.16^\circ$ of the Sample-A shows the presence of α - Fe_2O_3 , as it is the prominent peak related to the (104) plane similar results reported by (Lassoued et al., 2017). However, additional peaks located at $2^\circ\theta = 24.18^\circ, 35.68^\circ, 49.48^\circ$ and 54.10° could not be linked to any diffracted intensity of Fe_2O_3 planes. According to (Justus et al., 2016) the additional peaks, the FeO_2 and FeO phases of iron oxide can be associated.

The XRD patterns of hematite are shown in Fig. 2(b). hematite has eight prominent strong peaks which labeled with d spacing. Here, considered both Samples-A as well as Samples-B have same crystal structures. However, the peak intensities of the Sample-A are greater than Sample-B as prepared via co-precipitation method, the thin peaks behaviors which reflects the crystallite size of the particles result relates with a $\gamma \rightarrow \alpha$ - Fe_2O_3 phase alteration, that occurred during calcination process at 500°C and the faint peaks were seen at d-spacing of 2.86, 2.030, 1.7921, 1.5704 and 1.5382 Å, correspond to (phase rhombohedral structure) moderate crystalline of α - Fe_2O_3 was identified (Kumar et al., 2008). Low intense peaks confirm the phase formation of Fe_2O_3 , however position of intense peak at $d = 2.4724$ Å corresponds to the FeO_2 phase imply that the formation of Fe_2O_3 was not complete.

The XRD patterns of Sample-B represent in Fig. 2(b) composed of completely crystalline γ - Fe_2O_3 (minor phase, cubic, and spinel structure) and α - Fe_2O_3 (major phase) with an increase in the height of the peak which are linked to all the phases which formed the crystallization degree enhancement of α - Fe_2O_3 and γ - Fe_2O_3 reported by (Chaudhari et al., 2009).

The unit cell of α - Fe_2O_3 is hexagonal and consists only octahedral coordinated Fe^{3+} ions similar arguments reported by these researchers (Deraz et al., 2012). Eqs. (1)–(6) was used to derive the lattice parameters and other physical measurement. The lattice parameters of the 'a' and 'c' was calculated at 5.0369 and 13.7637 Å on Sample-A and Sample-B shows 5.0378 and 13.7694 Å respectively (Table 1). The values are calculated and listed in Table 1. The synthesized sample has mashed phase, the calculated parameters $a = b = 5.4780$ Å, $c = 13.4216$ Å not relates with the given basic values. This might be due to the position of the shifted peak of the Fe_2O_3 lattice. The prepared samples have FeO and FeO_2 phases, minor change in the peak position results in the more changing in its lattice parameters. The structure of α - Fe_2O_3 NPs is shown in Fig. 2. Each Fe atom is surrounded by six oxygens forming FeO_6 octahedral. In α - Fe_2O_3 , the location of oxygen atom can be considered as approximating hexagonal close packing reported by (Sharma et al., 2020).

In contrast, crystallite size was measured by Debye-Scherrer's Eq.3 and found in nanometer range. The Sample-A have 33 nm as compared to Sample-B = 29 nm. The crystallite size was found 12% smaller of the Sample-B which is prepared by Sol-gel method. Similar results of crystallite size were reported by (Lassoued et al., 2017). The unit cell volume of the Sample-A is observed 301.8 Å while the Sample-B has 3007 Å which is least as compared to other Sample-B. Moreover, the dislocation density and X-ray density measured and obtained values listed in the Table 1. From XRD data to calculate and compared the ratios of peaks intensities (104)/(113) (Fe-occupancy)/(oxygen layers) (Zhao et al., 2007). The obtained results shows that both Sample-A and Sample-B have no appreciable changes in ratios of peaks (104)/(113) = 1.53. These results describe that the Sample-A and Sample-B may consist of the amorphous γ - Fe_2O_3 phase and nanocrystalline α - Fe_2O_3 phase. Another important observation of XRD scans all characteristic hematite peaks shift toward higher Bragg angles. This shift con-

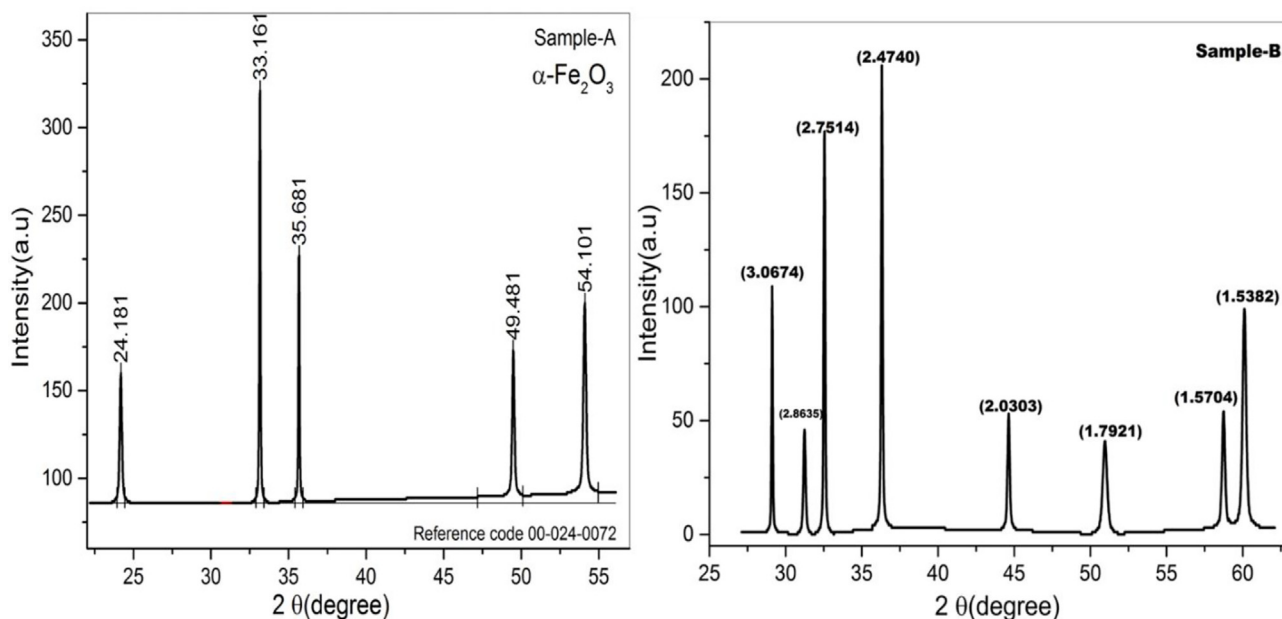


Fig. 2. XRD scans of hematite prepared from (a) co-precipitation (b) Sol-gel method.

Table 1
Structural Parameters of the Prepared Hematite $\alpha\text{-Fe}_2\text{O}_3$ nanoparticles.

Sample Details	Lattice Parameter	Volume of unit cell $\times 10^6 \text{ pm}^3$	Density g/cm^3	Crystallite Size nm	Dislocation density $\times 10^{15} \text{ lines}/\text{m}^2$	Micro strain
Sample -A	a = 5.0336 Å c = 13.7550 Å	301.8	5.27	33	0.918	0.0062
Sample- B	a = 5.0272 Å, c = 13.7540 Å	300.7	5.26	29	0.119	0.0084

firmly the change in the crystallite size and the crystallinity of the prepared Sample-A and Sample-B. As a result, we can conclude that the $\alpha\text{-Fe}_2\text{O}_3$ and $\gamma\text{-Fe}_2\text{O}_3$ phases in Sample-A are moderately crystalline. $\alpha\text{-Fe}_2\text{O}_3$, $\gamma\text{-Fe}_2\text{O}_3$, and Fe_3O_4 phases are present in Sample-B. (Sharma et al., 2020).

3.2. Morphology analysis

Fig. 3 represents the SEM images of Iron oxides nanoparticles synthesized by different two ways. Transformation of ferrihydrite using alkaline conditions results in hematite and goethite as a product, and hematite shows a wide variety of different shapes. In this study we observed that the SEM images of Sample-A as well as Sample-B indicate that the formation of particles with clusters or aggregates. Fig. 3(c-d) SEM images of hematite crystals are found grain size in the order of nanometers. The images of the synthesis material showed aggregated nature, and hematite particles dominate over other crystal morphologies.

3.3. Raman spectroscopy

Raman spectroscopy is a tool for the confirmation of phase purity and determines the crystalline and amorphous material qualities. The Raman spectra of the precursor and the end product are shown in Fig. 4(a to c), respectively. The hematite crystallizes in rhombohedra associated with the space group No.148 R-3. Five out of seven prominent bands of hematite verified by group theory having different intensities ($A_{1g} + E_g + 3T_{2g}$) surrounded by all sides and four active infrared modes.

The A_{1g} mode (490.68 cm^{-1}) and three E_g modes ($286, 403$ and 606 cm^{-1}). The bands which represent the hematite are around 228.6 cm^{-1} and 295.02 cm^{-1} and it was located in our spectrum

at (286 cm^{-1} and 291 cm^{-1}). The band near to 1313.85 cm^{-1} is a vibration which is due to unclear origin according to literature reported that the band 1313.85 cm^{-1} results from the scattering of two magnons exist in the structure, and (Chernyshova et al., 2007) reported that this process was due to second harmonic vibration of phonon. The bands in the Raman spectrum that are present 600 to 700 cm^{-1} in both the experimental and theoretical spectrums differ because the relative intensities are inverted. This variation shows the existence of $\gamma \rightarrow \alpha\text{-Fe}_2\text{O}_3$ and Fe_3O_4 in the sample having different phases. Additionally, in the spectrum related to experimental value does not appear which is according to the previous variation. There are two important and useful crystalline types of Fe_2O_3 first one is maghemite having cubic structure and hematite with the rhombohedral structure.

The variation in phase in $\gamma \rightarrow \alpha\text{-Fe}_2\text{O}_3$ occur in calcination process at about $500 \text{ }^\circ\text{C}$. The variation in phase which took place during calcination gives $\alpha\text{-Fe}_2\text{O}_3$ powder with significant grain growth and aggregation. (Bersani et al., 1999) reported disorder in the structure of hematite at the very initial stage of nanocrystalline material (ferrihydrite). For instance, if the origin of hematite is amorphous material from which it was changed into crystallized than it is possible to some extent that disorder in structure may be observed in crystalline hematite. Disorder may be lack of long range order and large number of atoms in layer surface.

3.4. UV-Vis studies

UV-Vis absorption spectrum was done for chemically synthesized Iron oxides $\alpha\text{-Fe}_2\text{O}_3$ at room temperature are shown in Fig. 5. It can be observed that synthesized Iron oxides exhibit absorption bands observed for different Sample-A and Sample-B. The peak at $562, 674$ and 902 nm were assigned to the pair excita-

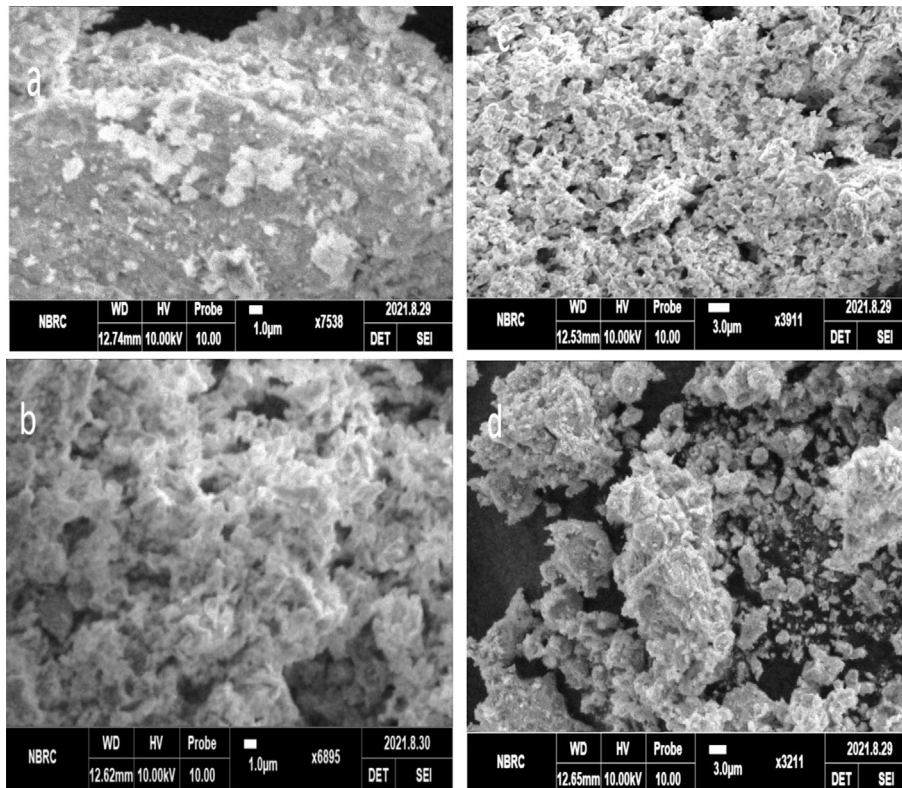


Fig. 3. SEM images of hematite nanoparticles α -Fe₂O₃ (a) co-precipitation (b) Sol-gel.

tion processes, these are ligand field transitions and the charge transfer band tails (Gao et al., 2012). In the present work, optical indirect and direct band gap energy (E_g) can be measured with using the Tauc equation.

$$(\alpha h\nu)^{\frac{1}{n}} = -B(h\nu - E_g) \quad (10)$$

where, 'hv' denotes the incident photon energy in electron volt, ' α ' represents absorption coefficient of the material, B is the constant which depends on material and E_g is optical band gap, and n may have different values according to direct allowed, indirect, forbidden and indirect forbidden transitions.

Tauc plots are shown in Fig. 5(b and c) the band gap energy can be calculated by the intercept of the plot of $(\alpha h\nu)^{\frac{1}{n}}$ versus 'hv'. The average band gap is determined by extrapolating the curve's linearly component. The mean band gap energy is found of the Sample-A and Sample-B is 2.4 eV for similar spherical and for quasi-cubic samples (Shebanova et al., 2003).

It has been observed that the band gap of an any material based on crystal structure as well as particle size of the material. It has been reported that α -Fe₂O₃ may exhibits direct and indirect band gaps (Jubb et al., 2010). The direct and indirect band gaps of α -Fe₂O₃ in the literature are obtained to be closely related to 2.15 eV and 1.87 eV, respectively (Akl et al., 2004). The final results represent the blue shifts when it was made a comparison with the bulk α -Fe₂O₃, that may be the effect of quantum size. (Akl et al., 2012). Shape dependent effect due to possible orientation in single axis is an important key factor of optical properties. α -Fe₂O₃ nanoparticles mostly show unusual magnetic properties.

3.5. I-V characterization

Two probe method was used with the help of Keithley Electrometer Model 2401 for I-V characterization of Iron oxide α -

Fe₂O₃. Pellets of Iron oxide were fabricated with particular dimensions. Fig. 6(a) shows a family of I-V curves in slope Sample-A was measured between 323 and 873 K temperatures. The electric resistivity of the given samples measured by using relation:

$$R = \rho L/A \quad (11)$$

where A is the area, L is width and R is resistance of pellet. The value of electrical resistivity depends on configuration of synthesized samples and the crystal structure. The electrical resistivity was found 4.61×10^9 (Ω .cm). Iron oxide α -Fe₂O₃ specimens have shown semi-conducting nature. Fig. 6. shows the trends of electrical resistivity depending on variations in temperatures. The graph advocates that log of resistivity increases and then starts decreasing till to 873 K. Also the samples are intensively applicable in the field of telecommunication 10^8 (Ω .cm) and low resistive devices like transformers to manage eddy current losses.

3.6. Dielectric properties

3.6.1. Frequency dependence of dielectric constant and dielectric loss tangent ($\tan \delta$)

In the present study, the dielectric parameters namely dielectric constant, loss tangent and AC conductivity were measured at room temperature synthesized sample by sol gel and coprecipitation method. Both the dielectric constant and dielectric loss tangent ($\tan \delta$) have high value at higher frequency is caused by space charge polarisation. From the Fig. 7, it is observed that the dielectric constant and dielectric loss tangent values of the Sample-A and Sample-B remains constant behaviour in the high frequency region and applied electric field lagbehind the frequency. Therefore, Maxwell-Wagner interfacial type polarisation helps explain the dielectric trend (Liu et al., 2004).

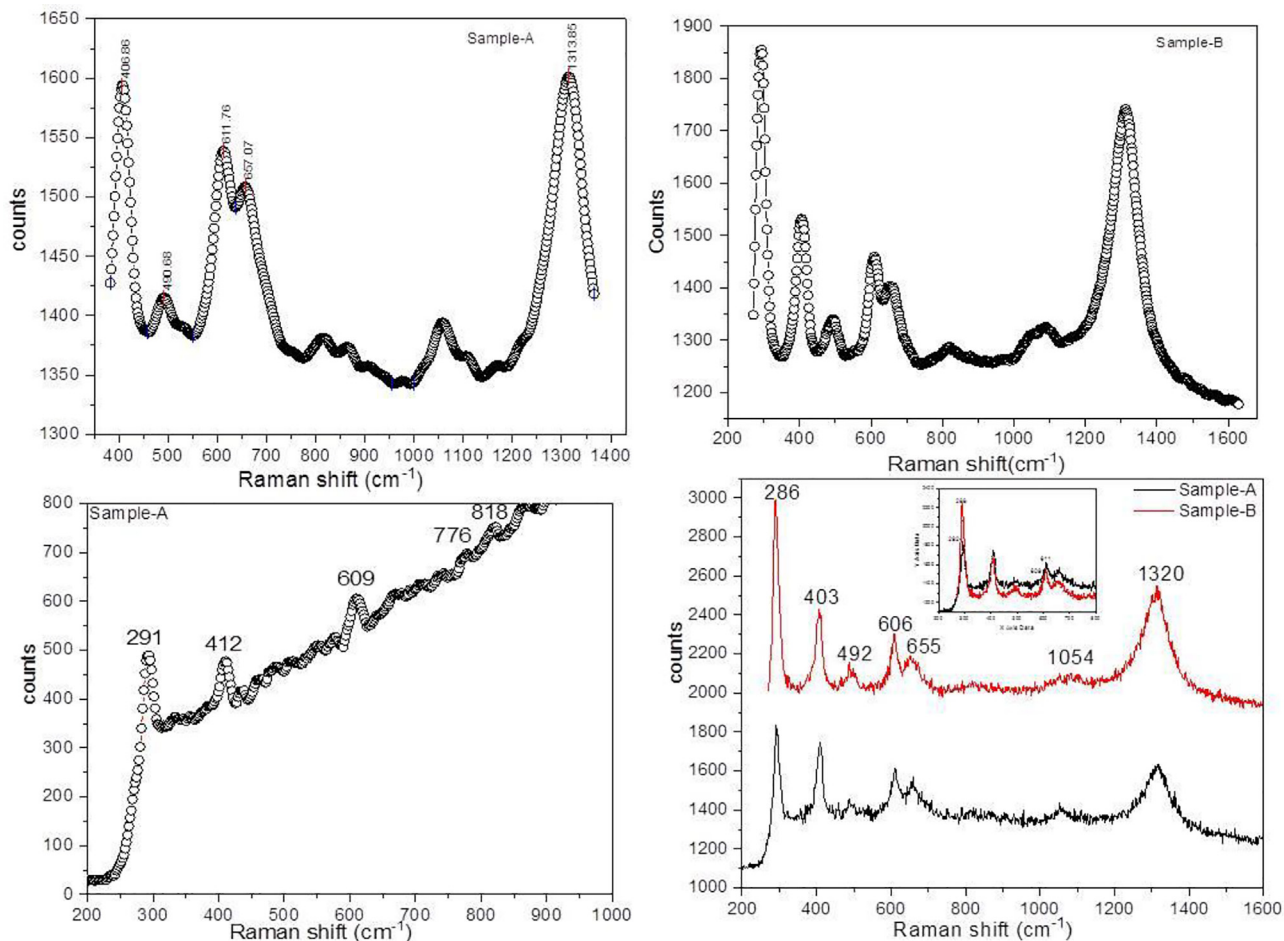


Fig. 4. Raman spectra of the precursor (a) co-precipitation (b) Sol-gel.

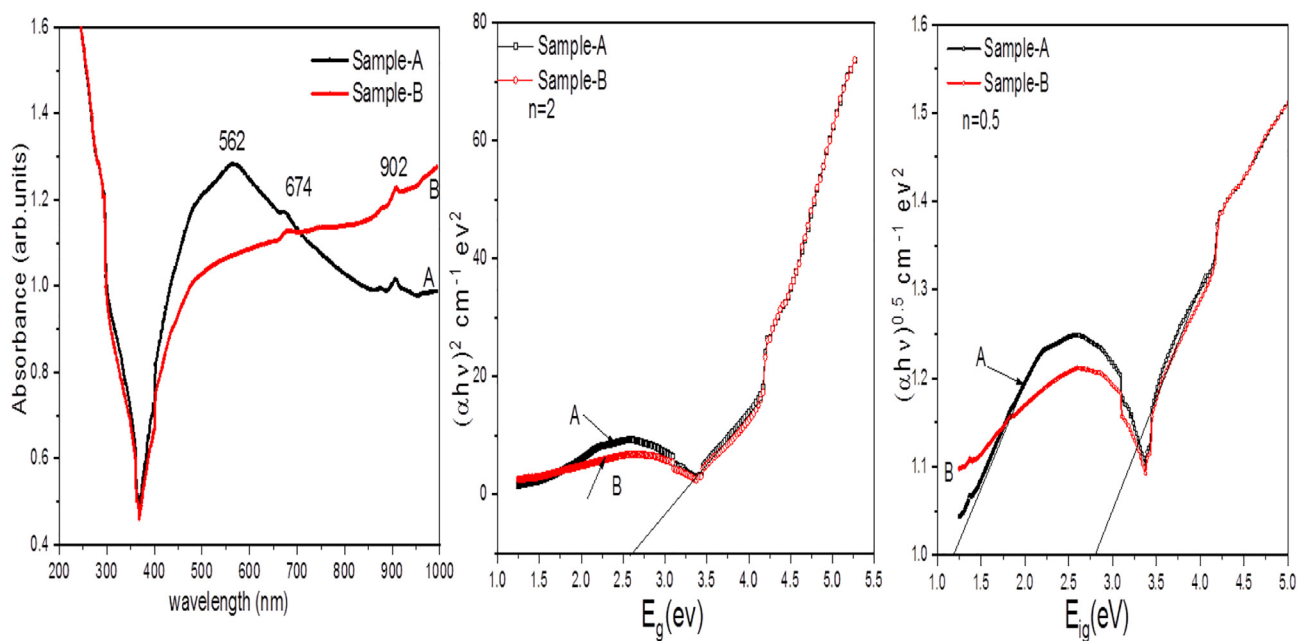


Fig. 5. (a) UV-vis absorption spectra of the synthesized α -Fe₂O₃ NPs (b&c) Variation of $(\alpha h\nu)^n$ ($n = 0.5$ and 2) Vs photon energy E_g (eV).

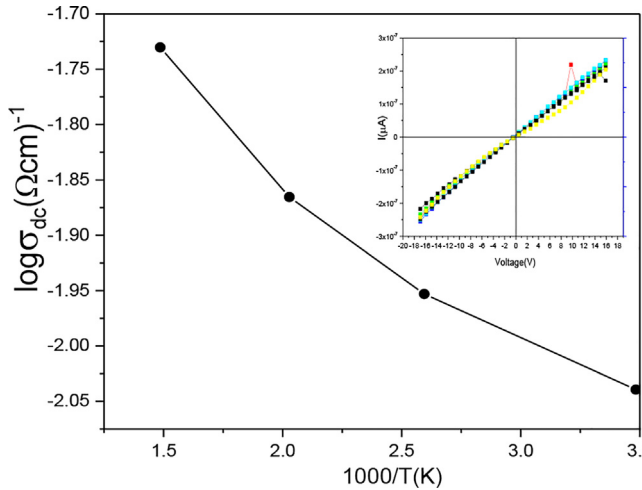


Fig. 6. (insight) I-V characteristics (a) log Resistivity Vs 1000/T(k).

3.6.2. AC-conductivity

Fig. 8 indicates the electrical conductivity of Iron oxides is only because of the Electron hopping between ions of the same element can occur in many valence states. Conductivity of Sample-A increased by increasing the frequency expressed a normal behavior. Therefore, It adheres/relates to a Power Law, which can be written as $\sigma_{ac} = A\omega^n$. Here A is the constant which depends on the Temperature with conductivity units ohm.cm^{-1} . The ω is the angular frequency and n is the constant its value varies from 0 to 1 which give the all information associated to material properties and more variation in properties occurs with increasing ion-ion interaction (Xu et al., 2005). It is concluded that the behavior of ac conductivity at low frequencies is influenced by the grain surface, whereas dispersion at high frequencies may be related to grain conductivity (Yuan et al., 2006).

3.7. MH-loop analysis

Fig. 9 represents the magnetic hysteresis loops of the synthesized samples at room temperature. The results showed the satura-

tion magnetization (Ms) Sample-A have 9.89 emu while Sample-B 1.72 emu. The values of remanent magnetization (Mr) Sample-A have 4.63 emu as compared to Sample-B 0.65 emu and coercivity (Hc) observed of the Sample-A 1404(G) as well as Sample-B have the coercivity (Hc) 1040(G). Moreover, the sample displayed the highest magnetic properties and based on the microstructure variations. It may be due to the effect of possible orientation in single axis. Therefore, magnetization also depend on the shape of Fe_2O_3 samples. The variation of the magnetic parameters also depends upon the method of preparation of prepared samples. The arrangement pattern of Fe^{3+} ions produce the pair of FeO_6 octahedral attached with Fe^{3+} ions coupled by antiferromagnetic behavior by the shared octahedral faces also with c-axis of unit cell.

Two inter-penetrating antiferromagnetic sub lattices can be found in the basal plane which results in ferromagnetic interaction (Zhang et al., 2009).

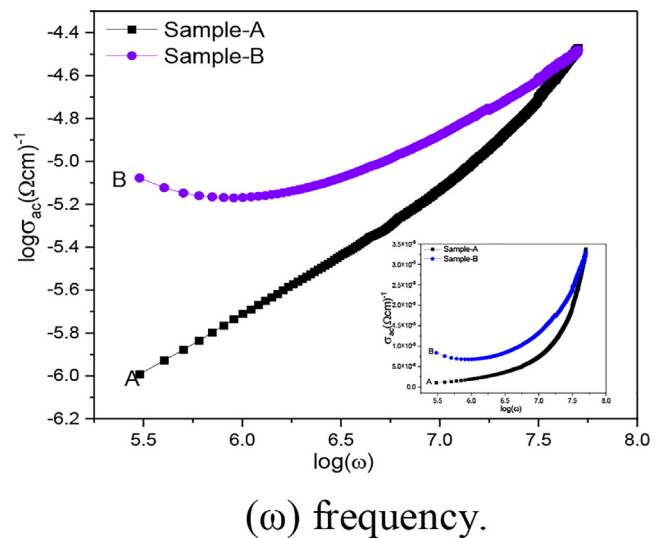


Fig. 8. Variation of ac conductivity (σ_{ac}) with log (ω) frequency.

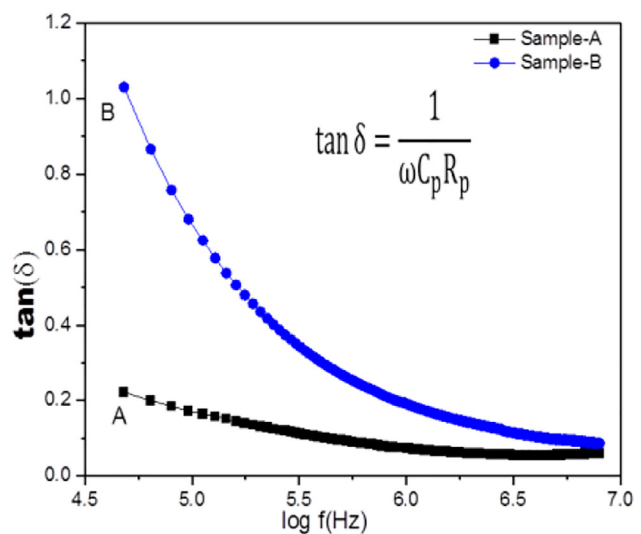
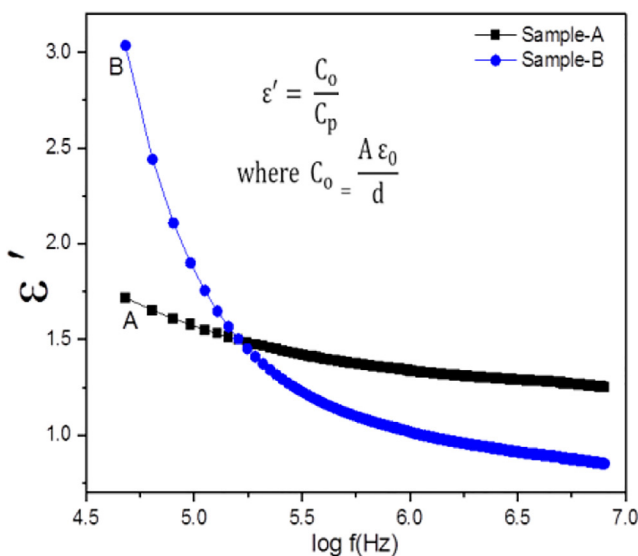


Fig. 7. Variation on the (a) Dielectric constant and (b) Dielectric loss tangent Vs frequency.

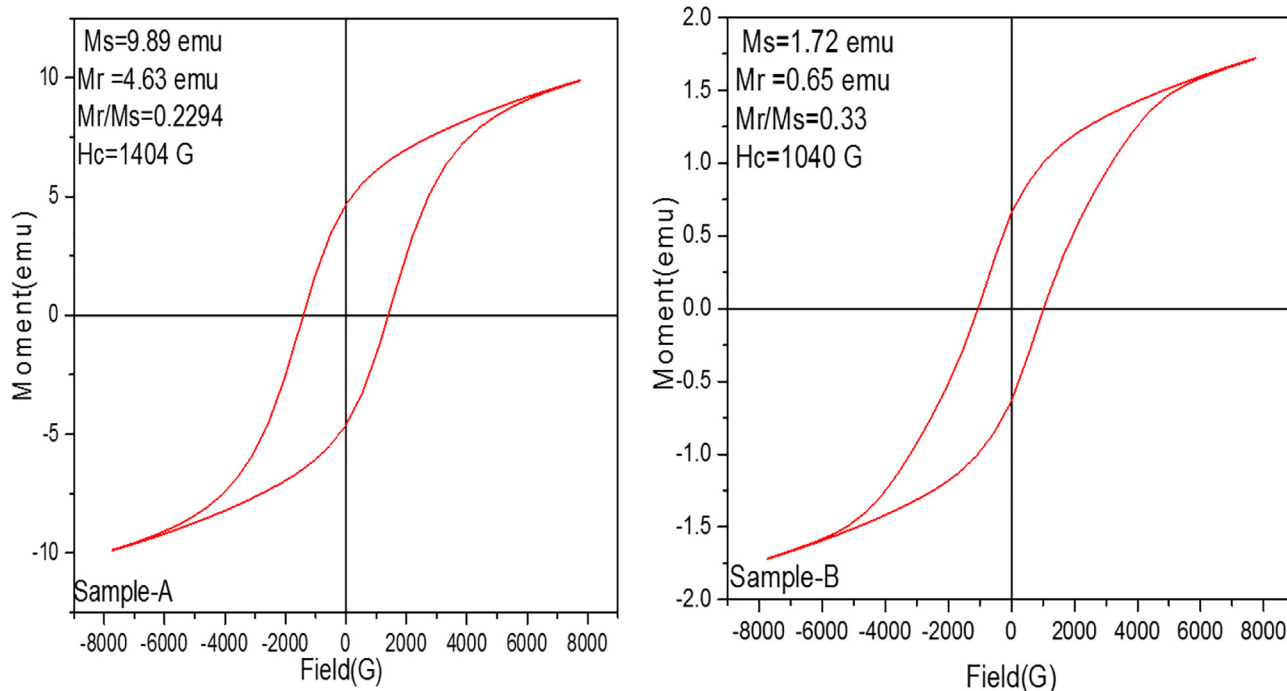


Fig. 9. M–H loops of prepared α -Fe₂O₃ nanoparticles observed at room temperature.

4. Conclusions

In summary, the hematite a particle including α -Fe₂O₃ NP with distinct size and shape has been successfully prepared via the Sol-gel and co-precipitation method. The microstructural study was done by the most using technique XRD. Scherrer's formula was used to calculate the crystallite size, Sample-A, have 33 nm while the Sample-B = 29 nm which is 12% smaller as compared to Sample-B which is prepared by Sol-gel method. The SEM analysis was shows the morphology of the material. Tauc plot is employed to estimate the optical band gap energy. In particular, the Sample-A is showing the transition in phase from goethite to hematite consequently change in the bandgap and structure. Thermal effect on, Iron oxides nanoparticles is showing bandgap decreased and transferred the phase from goethite to hematite. The Maxwell-Wagner polarisation model is used to predict changes in the dielectric constant and loss tangent with frequency. Materials with low dielectric loss can be used to make high frequency devices. The magnetic behavior of the sample-A observed dominate Ms = 9.29 emu and coercivity Hc = 1404(G) as compared to Sample-B. The synthesized materials can be used in many applications such as catalysis, sensors and water purification.

Declaration of Competing Interest

The authors declare that they have no known competing financial interests or personal relationships that could have appeared to influence the work reported in this paper.

Acknowledgement

Researchers Supporting Project number (RSP2023R397), King Saud University, Riyadh, Saudi Arabia

Appendix A. Supplementary material

Supplementary data to this article can be found online at <https://doi.org/10.1016/j.jksus.2023.102695>.

References

- Abbas, G., Rasul, A., Alam, M.F., Saadullah, M., Muzammil, S., Iqbal, O., Atif, M., Hanif, M., Shah, S., Ahmad, S., Shafiq, S., Afzal, M., 2022. Nanoparticles of thiolated chitosan for controlled delivery of moxifloxacin: in-vitro and in-vivo evaluation. *J. King Saud. Univ. Sci.* 34 (7), 102218.
- Alam, M.F., Shafiq, Z., Mahmood, A., Atif, M., Anwar, H., Hanif, A., Yaqub, N., Farooq, W.A., Fatehmulla, A., Ahmad, S., Elgawad, A.E., Alimgeer, K.S., Gia, T.N., Ahmed, H., 2021. Assessment of green and chemically synthesized copper oxide nanoparticles against hepatocellular carcinoma. *J. King Saud Univ. Sci.* 33, 101669.
- Assefa, A.T., Ahmed, G.M.S., Alamri, S., Edacherian, A., Jiru, M.G., Pandey, V., Hossain, N., 2022. Experimental investigation and parametric optimization of the tungsten inert gas welding process parameters of dissimilar metals. *Materials* 15 (13), 4426.
- Atif, M., Fakhar-e-Alam, M., Firdous, S., Zaidi, S.S.Z., Suleman, R., Ikram, M., 2010. Study of the efficacy of 5-ALA mediated photodynamic therapy on human rhabdomyosarcoma cell line (RD). *Laser Phys. Lett.* 7 (10), 757–764.
- Atif, M., Fakhar-e-Alam, M., Sabino, L.G., Ikram, M., De Araujo, M.T., Kurachi, C., Alsalhi, M.S., 2011. Analysis of the combined effect of lasers of different wavelengths for PDT outcome using 600, 630, and 660 nm. *Laser Phys. Lett.* 8 (5), 386–392.
- Atif, M., Iqbal, S., Ismail, M., Mansoor, Q., Mughal, L., Aziz, M.H., Farooq, W.A., 2019. Manganese-doped cerium oxide nanocomposite induced photodynamic therapy in MCF-7 cancer cells and antibacterial activity. *BioMed. Res. Int.*
- Atif, M., Iqbal, S., Fakhar-e-Alam, M., Mansoor, Q., Alimgeer, K.S., Fatehmulla, A., Chu, Y.M., 2021. Manganese-doped cerium oxide nanocomposite as a therapeutic agent for MCF-7 adenocarcinoma cell line. *Saudi J. Biol. Sci.* 28 (2), 1233–1238.
- Bersani, D., Lottici, P.P., Montenero, A., 1999. Micro-Raman investigation of iron oxide films and powders produced by Sol-gel syntheses. *J. Raman Spectrosc.* 30 (5), 355–360.
- Chaudhari, N.K., Kim, H.C., Son, D., Yu, J.S., 2009. Easy synthesis and characterization of single-crystalline hexagonal prism-shaped hematite α -Fe₂O₃ in aqueous media. *Cryst Eng Comm* 11 (11), 2264–2267.

- Chernyshova, I.V., Hochella Jr., M.F., Madden, A.S., 2007. Size-dependent structural transformations of hematite nanoparticles. 1. Phase transition. *Phys. Chem. Chem. Phys.* 9 (14), 1736–1750.
- Deraz, N.M., Alarifi, A., 2012. Novel processing and magnetic properties of hematite/maghemite nano-particles. *Ceram. Int.* 38, 4049–4055.
- Fakhar-e-Alam, M., Aseer, M., Rana, M.S., Aziz, M.H., Atif, M., Yaqub, N., Farooq, W.A., 2020a. Spectroscopic features of PHOTOGEN[®] in human Rhabdomyosarcoma (RD) cellular model. *J. King Saud Univ.-Sci.* 32 (7), 3131–3137.
- Fakhar-e-Alam, M., Atif, M., Alimgeer, K.S., Rana, M.S., Yaqub, N., Farooq, W.A., Ahmad, H., 2020b. Synergistic effect of TEMPO-coated TiO₂ nanorods for PDT applications in MCF-7 cell line model. *Saudi J. Biol. Sci.* 27 (12), 3199–3207.
- Fakhar-e-Alam, M., Saddique, S., Hossain, N., Shahzad, A., Ullah, I., Sohail, A., Saadullah, M., 2022. Synthesis, characterization, and application of BaTiO₃ nanoparticles for anti-cancer activity. *J. Cluster Sci.*, 1–11.
- Gao, X., Lu, Y., Xing, Y., Ma, Y., Lu, J., Bao, W., Wang, Y., Xi, T., 2012. A novel anticancer and antifungus phenazine derivative from a marine actinomycete BM-17. *Microbiol. Res.* 167 (10), 616–622.
- Goldman, A., 2006. A Green approach: synthesis, characterization and opto-magnetic properties of Mg_{0.5}Mn_{1-x}Fe₂O₄ spinel nanoparticles. *Ferrite Technology*, 2nd ed., Springer Publication, 83–135.
- Graca, M.P.F., Ferreira da Silva, M.G., Sombra, A.S.B., Valente, M.A., 2007. Electric and dielectric properties of a SiO₂-Na₂O-Nb₂O₅ glass subject to a controlled heat-treatment process. *Physica B* 396, 62–69.
- Gunjo, D.G., Yadav, V.K., Sinha, D.K., Elkotb, M.A., Ahmed, G.M.S., Hossain, N., Abdelmohimen, M.A., 2022. Improvement in thermal storage effectiveness of paraffin with addition of aluminum oxide nanoparticles. *Materials* 15 (13), 4427.
- Hassan, S.M., Karam, W., Alam, M.F., 2022a. Physical properties of PEG coated Y doped ZnO nanoparticles and their potential as high gamma dose thermoluminescence material. *J. King Saud Univ. Sci.* 34, 101958.
- Hassan, S.M., Siddique, M.T., Alam, M.F., Atif, M., Saifullah, A., Marwat, N., Khurshid, A., Obaidullah, N., Hossain, N., Ahmad, S., Alimgeer, K.S., 2022b. Hydrothermally synthesized lanthanide-incorporated multifunctional zirconia nanoparticles: Potential candidate for multimodal imaging. *J. King Saud Univ. Sci.* 34, 10208.
- Jubb, A.M., Allen, H.C., 2010. Vibrational Spectroscopic characterization of hematite, maghemite, and magnetite thin films produced by vapor deposition. *ACS Appl. Mater. Interfaces* 2 (10), 2804–2815.
- Justus, J.S., Roy, S.D.D., Raj, A.M.E., 2016. Synthesis and characterization of hematite nanopowders. *Mater. Res. Express* 3, (10) 105037.
- Kanungo, S.B., Mishra, S.K., 1996. Thermal dehydration and decomposition of FeCl₃·H₂O. *J. Thermal Anal.* 46, 1487–1500.
- Khollam, Y.B., Dhage, S.R., Potdar, H.S., Deshpande, S.B., Bakare, P.P., Kulkarni, S.D., Date, S.K., 2002. Microwave hydrothermal preparation of submicron-sized spherical magnetite (Fe₃O₄) powders. *Mater. Lett.* 56 (4), 571–577.
- Kumar, V., Rana, A., Yadav, M.S., Pant, R.P., 2008. Size-induced effect on nano-crystalline CoFe₂O₄. *J. Magn. Magn. Mater.* 320 (11), 1729–1734.
- Lassoued, A., Lassoued, M.S., Dkhil, B., Gadri, A., Ammar, S., 2017. Synthesis, structural, optical and morphological characterization of hematite through the precipitation method: effect of varying the nature of the base. *J. Mol. Struct.* 1141, 99–106.
- Liu, J., Duan, C.G., Yin, W.G., Mei, W.N., Smith, R.W., Hardy, J.R., 2004. Large dielectric constant and Maxwell-Wagner relaxation in Bi₂/3Cu₃Ti₄O₁₂. *Phys. Rev. B* 70, (14) 144106.
- Mahmood, A., Munir, T., Alam, M.F., Atif, M., Shahzad, K., Alimgeer, K.S., Gia, T.N., Ahmed, H., Ahmad, S., 2022. Analyses of structural and electrical properties of aluminium doped ZnONPs by experimental and mathematical approaches. *J. King Saud Univ. Sci.* 34, 101796.
- Mustafa, G., Islam, M.U., Zhang, W., Jamil, Y., Iqbal, M.A., Hussain, M., Ahmad, M., 2015a. Temperature dependent structural and magnetic properties of Cerium substituted Co-Cr ferrite prepared by auto-combustion method. *J. Magn. Magn. Mater.* 378, 409–416.
- Mustafa, G., Islam, M.U., Zhang, W., Anwar, A.W., Jamil, Y., Murtaza, G., Ahmad, M., 2015b. Influence of the divalent and trivalent ions substitution on the structural and magnetic properties of Mg_{0.5-x}Cd_xCo_{0.5}Cr_{0.04}Tb_yFe_{1.96-y}O₄ ferrites prepared by sol-gel method. *J. Magn. Magn. Mater.* 387, 147–154.
- Nosheen, S., Iqbal, S.S., Sabir, A., Alturki, A., Hossain, N., Bahadar, A., 2022. Synthesis and characterizations of novel spinel ferrites nanocomposites A₁₀₋₅Cr₀₋₅Zn₀Fe₂O₄ and Zn₀₋₅Cr₀₋₅A₁₀Fe₂O₄. *J. Cluster Sci.*, 1–6.
- Peña-Bahamonde, J., Nguyen, H.N., Fanourakis, S.K., Rodrigues, D.F., 2018. Recent advances in graphene-based biosensor technology with applications in life sciences. *J. Nanobiotechnol.* 16 (1), 1–17.
- Sharma, D., Ledwani, L., Mehrotra, T., Kumar, N., Pervaiz, N., Kumar, R., 2020. Biosynthesis of hematite nanoparticles using Rheum emodi and their antimicrobial and anticancerous effects in vitro. *J. Photochem. Photobiol. B: Biol.* 206, 111841.
- Shebanova, O.N., Lazor, P., 2003. Raman spectroscopic study of magnetite (FeFe₂O₄): a new assignment for the vibrational spectrum. *J. Solid State Chem.* 174 (2), 424–430.
- Xu, Q., Chen, X., Chen, W., Chen, S., Kim, B., Lee, J., 2005. Synthesis, ferroelectric and piezoelectric properties of some (Na_{0.5}Bi_{0.5})TiO₃ system compositions. *Mater. Lett.* 59 (19–20), 2437–2441.
- Yuan, G.L., Baba Kishi, K.Z., Liu, J.M., Wing, S.O.S., Wang, Y.P., Liu, Z.G., 2006. Multiferroic properties of single-phase Bi_{0.8}5La_{0.15}FeO₃ lead-free ceramics. *J. Am. Ceram. Soc.* 89 (10), 3136–3319.
- Zhang, S.T., Kouna, A.B., Jo, W., Jamin, C., Seifert, K., Granzow, T., Rodel, J., Damjanovic, D., 2009. High-Strain lead free antiferroelectric electrostrictor S. *Adv. Mater.* 21 (46), 4716–4720.
- Zhao, B., Wang, Y., Guo, H., Wang, J., He, Y., Jiao, Z., Wu, M., 2007. Iron oxide (III) nanoparticles fabricated by electron beam irradiation method. *J. Wang Sci. Poland* 25 (4).